



## Research paper

# Photocatalytic activity enhancement of core-shell structure $g\text{-C}_3\text{N}_4@\text{TiO}_2$ via controlled ultrathin $g\text{-C}_3\text{N}_4$ layer

Yingying Wang<sup>a</sup>, Wenjuan Yang<sup>a,b</sup>, Xianjie Chen<sup>a</sup>, Jun Wang<sup>a</sup>, Yongfa Zhu<sup>a,\*</sup><sup>a</sup> Department of Chemistry, Tsinghua University, Beijing 100084, China<sup>b</sup> School of Chemistry and Chemical Engineering, Yulin University, Yulin City 719000, Shaanxi, China

## ARTICLE INFO

## Article history:

Received 13 June 2017

Received in revised form 21 July 2017

Accepted 1 August 2017

Available online 2 August 2017

## Keywords:

Photocatalysis

 $\text{TiO}_2$ Ultrathin  $g\text{-C}_3\text{N}_4$ 

Core-shell structure

Layer-dependent effect

## ABSTRACT

The  $g\text{-C}_3\text{N}_4@\text{TiO}_2$  core-shell structure photocatalysts with controlled ultrathin  $g\text{-C}_3\text{N}_4$  layer (0 nm, 1.0 nm, 1.5 nm, 3.0 nm) were prepared by a new method of the sol-gel approaches *in situ* coating re-assembled. The  $g\text{-C}_3\text{N}_4@\text{TiO}_2$  sample with 1.0 nm thickness of shell layers has the highest visible light photocatalytic degradation phenol activity which is almost 7.2 times as high as that of bulk  $g\text{-C}_3\text{N}_4$ . The highest photocurrent response intensity is increased by ten times higher than that of  $g\text{-C}_3\text{N}_4$  and five orders of magnitude compare to  $\text{TiO}_2$ . The removal rate of phenol using  $g\text{-C}_3\text{N}_4@\text{TiO}_2$  core-shell catalyst is 30% and the degree of mineralization by the same catalyst is 19.8%, which dramatically increase compared with that of  $g\text{-C}_3\text{N}_4$  and  $\text{TiO}_2$ . The enhanced performance of the degradation phenol and the mineralization is owing to effective charge separation revealed by the photoluminescence (PL), electrochemical impedance spectroscopy (EIS) and density functional theory calculations (DFT), superoxide radicals as the main oxidative species proved by electron spin resonance spectroscopy (ESR). And the core-shell structure could effectively promote the electron transfer from  $g\text{-C}_3\text{N}_4$  to  $\text{TiO}_2$  during the catalytic process. The results of repetitive experiment and cycle experiment show that the  $g\text{-C}_3\text{N}_4@\text{TiO}_2$  has a strong binding force between the core and shell, which is stable, without secondary pollution and convenient for recovery. What's more, the results revealed the law between the different  $g\text{-C}_3\text{N}_4$  shell layers (0 nm, 1.0 nm, 1.5 nm, 3.0 nm) over the  $g\text{-C}_3\text{N}_4@\text{TiO}_2$  samples and the corresponding catalytic activity, which successfully established the structure-activity relationship. A new catalytic concept namely layer-dependent effect was found, that is number of layers over  $g\text{-C}_3\text{N}_4$  of the core-shell structure determines photocatalytic activity.

© 2017 Elsevier B.V. All rights reserved.

## 1. Introduction

The development of sunlight harvesting catalytic materials is the key target in photocatalysis field [1], and the most commonly used photocatalytic material is inorganic semiconductors including metal oxides, nitrides, sulfides and so on. However, the application of such materials is seriously limited, because these photocatalysts are greatly suffering from photocorrosion under sunlight irradiation and unable to control the extinction coefficient and difficult to broaden the spectral response range [2]. In order to overcome the bottleneck, the researchers recently successfully introduce all-organic semiconductor materials into the field of photocatalysis [3]. Among all the organic semiconductor materials,  $g\text{-C}_3\text{N}_4$  is an attractive organic semiconductor photocatalyst, which is firstly reported by Wang et al. to split water into hydrogen gas under

visible light irradiation [4]. Then  $g\text{-C}_3\text{N}_4$  as a star material in the field of photocatalysis has been widely concerned by scientists owing to its outstanding visible light activity, thermal and chemical stability, which is applied to the degradation of organic pollutants [5], production of hydrogen [6] and oxygen from water [7] and photocatalytic conversion of  $\text{CO}_2$  [8] under visible light. However, some shortcomings seriously confine its wide application, including fast recombination of photoinduced carriers [9], inefficient utilization of visible light, difficult to be separated from water completely [10], dissolution caused secondary pollution [11]. How to solve these problems to achieve highly efficient photocatalysis remains a difficult challenge.

Considerable efforts have been directed towards the development of organic-inorganic polymer (MOFs) photocatalytic systems including  $\text{Cu}/\text{MIL}-101$  [12],  $\text{Au}@\text{Pd}/\text{UiO}-66$  [13] and  $g\text{-C}_3\text{N}_4$ -based hybrid photocatalytic systems including hybrid composite based on conjugated materials [14,15], 3D network structure hydrogels [16], transition metal doping [17,18], coupling with semiconductor [19,20]. Further improvements of the separation of

\* Corresponding author.

E-mail address: [zhuyf@mail.tsinghua.edu.cn](mailto:zhuyf@mail.tsinghua.edu.cn) (Y. Zhu).

photogenerated carriers and the availability of visible light are necessary. Among them, a large amount of work focuses on fabricating specific organic-inorganic composite structures which can make photogenerated electrons and holes separated in different components [21–23], such as  $g\text{-C}_3\text{N}_4/\text{Ag}$  [24], mesoporous  $g\text{-C}_3\text{N}_4/\text{ZnO}$  [25],  $g\text{-C}_3\text{N}_4/\text{BiPO}_4$  [26],  $g\text{-C}_3\text{N}_4/\text{Bi}_2\text{WO}_6$  [27] hybrid catalytic systems. The results found that the photocatalytic activities of these photocatalysts were greatly enhanced due to the formation of core-shell structure. There are many methods to form the core-shell structure, such as dipping method [9], ball milling method [28,29]. However, these traditional physical coating methods can't form a precisely controlled a few-layered  $g\text{-C}_3\text{N}_4$  coating on  $\text{TiO}_2$  nanostructure surface and the surface binding force between  $g\text{-C}_3\text{N}_4$  and  $\text{TiO}_2$  is not strong which restricts the efficient separation of photogenerated carriers in space leads to in low catalytic activity.

In this work, the finely controlled synthesis of a few-layered  $g\text{-C}_3\text{N}_4@\text{TiO}_2$  core-shell structure is achieved by using sol-gel approaches *in situ* coating re-assembled, which can promote the electron transfer between the core-shell and then regulate the photocatalytic activity so as to profoundly reveal the relationship between core-shell structure and photocatalytic activity [30]. The layers of the shell were well controlled by changing the calcination temperature and the concentration of CN colloidal suspension, which provided the catalytic materials with different shell thickness for systematical study. The  $g\text{-C}_3\text{N}_4@\text{TiO}_2$  sample with 1.0 nm shell thickness has the highest visible light photocatalytic activity which is almost 7.2 times as high as that of bulk  $g\text{-C}_3\text{N}_4$ . The degree of mineralization using  $g\text{-C}_3\text{N}_4@\text{TiO}_2$  core-shell catalyst is 19.8%, which dramatically increase compared with that of  $g\text{-C}_3\text{N}_4$  and  $\text{TiO}_2$ . The core-shell structure material can not only improve the degradation rate of phenol but also markedly improve the capability of mineralization. What's more, the results revealed the law between the absorbance capability over the  $g\text{-C}_3\text{N}_4@\text{TiO}_2$  sample with different thickness of  $g\text{-C}_3\text{N}_4$  shell layer and the corresponding catalytic activity, which successfully established the structure-activity relationship scrutinized by experiments and DFT calculations. The mechanism of the enhancement activity of  $g\text{-C}_3\text{N}_4@\text{TiO}_2$  core-shell structure and the active species in the catalytic process were elucidated by Raman spectroscopy, Infrared spectroscopy, Photoluminescence spectroscopy, Photocurrent and ESR characterization techniques. The results of repetitive experiment and cycle experiment show that the  $g\text{-C}_3\text{N}_4@\text{TiO}_2$  prepared by the sol-gel method has a strong binding force between the core and shell, which effectively reduces the dissolution of bulk  $g\text{-C}_3\text{N}_4$  material during the photocatalytic process and convenient for recovery.

## 2. Experimental

### 2.1. Preparation of $g\text{-C}_3\text{N}_4@\text{TiO}_2$ core-shell structure photocatalyst

Dicyandiamide was purchased from Beijing Chemical Reagent Corp., PR China;  $\text{TiO}_2$  (P25) was obtained from Degussa. All other reagents used in this research were analytical pure and used without further purification.

The  $g\text{-C}_3\text{N}_4$  was prepared by a typical pyrolysis of dicyandiamide in air atmosphere. The detailed preparation steps were as follows: 10 g dicyandiamide were put in a Muffle Furnace and heated to 550 °C at a heating rate of 2.3 °C/min and calcined at 550 °C for 4 h. The yield of the optimum  $g\text{-C}_3\text{N}_4$  was about 40%.

Preparation of CN colloidal suspension: Firstly, 1 g of  $g\text{-C}_3\text{N}_4$  powder was placed into a 100 mL flask and charged with reflux (the temperature of the refluxed condensate was room tempera-

ture). Then, 60 mL of 65 wt% of  $\text{HNO}_3$  was added and the mixture was heated at 80 °C for 3 h.

A certain amount of  $\text{TiO}_2$  powder was added to the CN sol. The solvent was slowly removed and the sample was dried at 150 °C. 50 wt%  $g\text{-C}_3\text{N}_4@\text{TiO}_2$  core-shell photocatalyst (400 °C, 450 °C, 500 °C, 550 °C and 600 °C) were obtained by annealing of 50 wt%  $g\text{-C}_3\text{N}_4@\text{TiO}_2$  samples at different temperatures in a tube furnace under  $\text{N}_2$  protection for 4 h. The  $g\text{-C}_3\text{N}_4@\text{TiO}_2$  samples (0.2 wt%, 0.6 wt%, 1 wt%, 5 wt%, 10 wt%, 15 wt%, 30 wt%) were calcined at 550 °C for 4 h to obtain  $g\text{-C}_3\text{N}_4@\text{TiO}_2$  photocatalyst with different mass fractions.

### 2.2. Characterizations

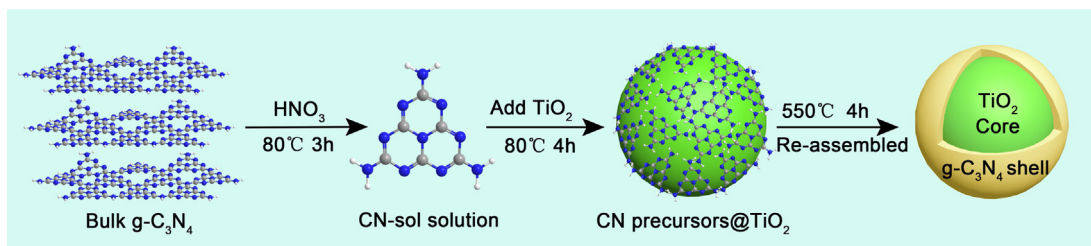
The morphologies of the  $g\text{-C}_3\text{N}_4@\text{TiO}_2$  core-shell photocatalyst were obtained by JEM 2010 electron microscope operated at an accelerating voltage of 100 kV. HRTEM were characterized by JEM-2011F field emission transmission electron microscopy with an accelerating voltage of 200 kV. The crystallinity of the  $g\text{-C}_3\text{N}_4@\text{TiO}_2$  photocatalyst were characterized by X-ray diffraction (XRD) by Rigaku D/max-2400 X-ray diffractometer with  $\text{Cu K}\alpha$  radiation ( $\lambda = 1.5406 \text{ \AA}$ ), the scanning range was 5–70°. The UV-vis diffuse reflectance spectroscopy were recorded on Hitachi UV-3010 UV-vis spectrophotometer, using  $\text{BaSO}_4$  as the reference sample. Fourier transform infrared spectra (FT-IR) were performed on Bruker VERTEX-70 spectrometer in the range of  $4000 \text{ cm}^{-1}$ – $600 \text{ cm}^{-1}$  with a resolution of  $1 \text{ cm}^{-1}$ . Raman spectra were carried out using a microscopic confocal raman spectrometer HORIBA HR 800 with an excitation of 785 nm laser light. Photoluminescence spectra were characterized by LS55 fluorescence spectrometer (Perkin-Elmer, USA) with a maximum excitation wavelength of 370 nm and a scanning wavelength range of 400–600 nm. The photocurrents were measured on an CHI 660 B electrochemical system. The active species of phenol degradation by  $g\text{-C}_3\text{N}_4@\text{TiO}_2$  core-shell structure catalyst can be detected on JEOL JES-FA200 EER electronic paramagnetic resonance spectrometer using DMPO (5,5-dimethyl-1-pyrroline N-oxide) as free radical trapping agent.

### 2.3. Photocatalytic experiments

The catalytic activity of  $g\text{-C}_3\text{N}_4@\text{TiO}_2$  core-shell structure photocatalyst was evaluated by the degradation of phenol in the static system in multtube agitated reactor XPA-7. Visible light source was obtained by a 500 W Xe lamp with a 420 nm cutoff filter, and the optical power density was maintained at an average of about  $23 \text{ mW/cm}^2$ . A typical process was as follows: 25 mg photocatalyst was added into 5 mg/L phenol solution, which was stirred under visible light irradiation. Take 3 mL of the reaction solution every 60 min and centrifuge to remove the photocatalytic material. The concentration of phenol contaminants was analysed by Shimadzu LC-20A high performance liquid chromatography (HPLC) with a Venusil XBP-C<sub>18</sub> and a UV detector operated at 270 nm. The mobile phase consisted of methanol and water (volume ratio: 60/40) at a flow rate of 1 mL/min.

### 2.4. Computational method

We carried out the calculations based on the density functional theory (DFT) with the Perdew–Burke–Ernzerh of [31] version of the generalized gradient approximation (GGA-PBE) for the exchange–correlation potential implemented in a plane-wave basis code VASP [32,33]. The pseudo-potential was described by the projector-augmented-wave (PAW) method [34]. An energy cut-off of 400 eV and  $5 \times 3 \times 1 \text{k-point}$  with a  $\Gamma$  centered k mesh were utilized in our calculations. The force on each atom was converged



**Scheme 1.** Schematic illustration of preparation of  $\text{g-C}_3\text{N}_4@\text{TiO}_2$  core-shell photocatalyst.

to  $0.02 \text{ eV}\text{\AA}^{-1}$  during the atomic structure optimization with a conjugate gradient (CG) [35] method. Standard DFT methods fail to acquire the correct electronic structure for strongly correlated systems such as Ti based material. To overcome the inaccuracy, GGA+U was utilized to correct the on-site Coulomb and exchange interactions for localized d orbitals of Ti. We choosed the  $U=3.0 \text{ eV}$  in this work accoding to the literature [36].

We constructed a model interface between anatase phase  $\text{TiO}_2$  and  $\text{g-C}_3\text{N}_4$ . The lattice constants of unit cell  $\text{TiO}_2$  area =  $b = 3.776 \text{ \AA}$ ,  $c = 9.486 \text{ \AA}$ ,  $\alpha = \beta = \gamma = 90^\circ$ . For  $\text{g-C}_3\text{N}_4$ , the lattice constants are  $a = b = 7.1515 \text{ \AA}$ ,  $c = 8.9864 \text{ \AA}$ . Here  $\text{TiO}_2$  (101) and  $\text{g-C}_3\text{N}_4$  (001) planes were selected owing to a small planar mismatch (less than 3%) between these two planes. At the interface, it preferred to form Ti-N, C—O—N bond due to the stronger dissociation energy.  $10.00 \text{ \AA}$  vacuum regions were set to avoid the interactions between top and bottom atoms in the periodic slab images.

### 3. Results and discussion

#### 3.1. Fabrication of core-shell structure

The  $\text{g-C}_3\text{N}_4@\text{TiO}_2$  core-shell structure photocatalysts with controlled ultrathin  $\text{g-C}_3\text{N}_4$  layer were fabricated by the sol-gel approaches *in situ* coating re-assembled illustrated in **Scheme 1**. Firstly, the bulk  $\text{g-C}_3\text{N}_4$  was prepared by a typical pyrolysis of dicyandiamide in air atmosphere [4]. Then, the  $\text{g-C}_3\text{N}_4$  bulk phase material was protonated by the process of strong oxidizing acid  $\text{HNO}_3$ , which is demonstrated as an efficient pathway for the sol processing of a stable  $\text{g-C}_3\text{N}_4$  colloidal suspension [30]. To generated the required number of  $\text{g-C}_3\text{N}_4$  layer on the outer surfaces of  $\text{TiO}_2$  nanostructure, a certain amount of  $\text{TiO}_2$  powder was added to the CN sol to fabricate uniformly CN precursors@ $\text{TiO}_2$  core-shell structure. The sample was re-polymerized in a tube furnace under

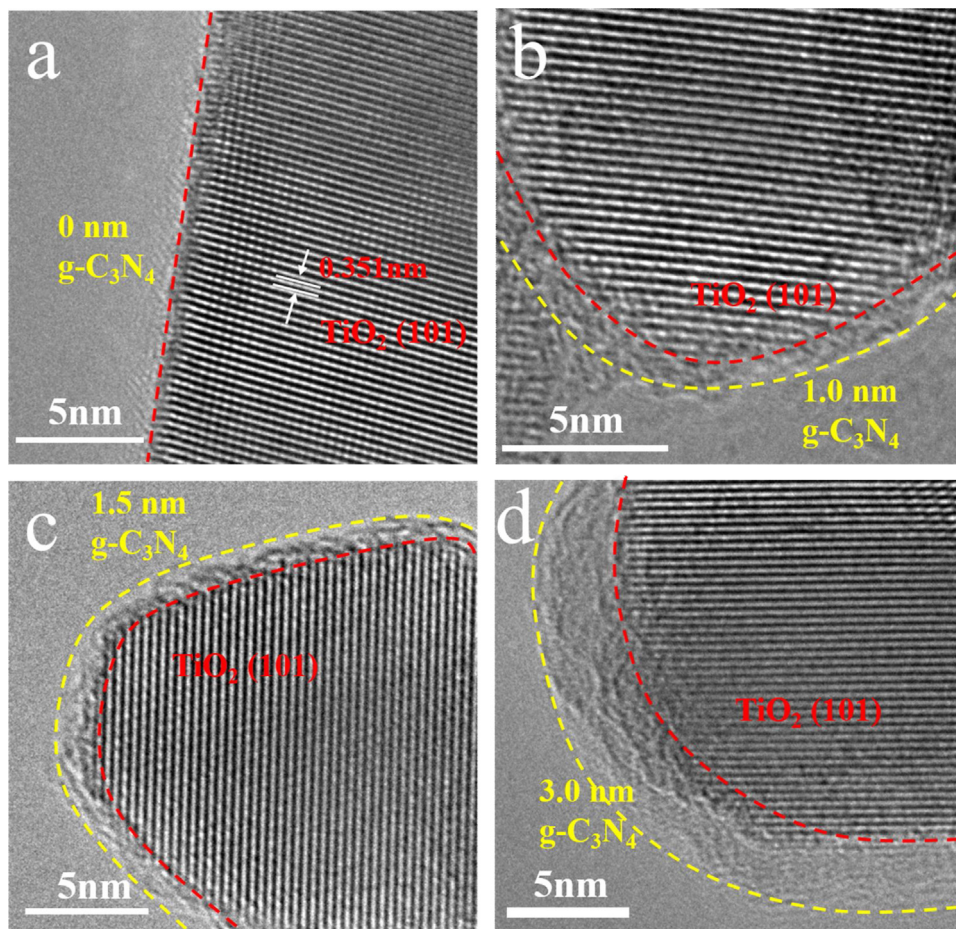


**Fig. 1.** HRTEM image of  $\text{TiO}_2$  and  $\text{g-C}_3\text{N}_4@\text{TiO}_2$  core-shell photocatalyst (a) pure  $\text{TiO}_2$ , (b) obtained at  $550^\circ\text{C}$ , (c) obtained at  $500^\circ\text{C}$  and (d) obtained at  $400^\circ\text{C}$ .

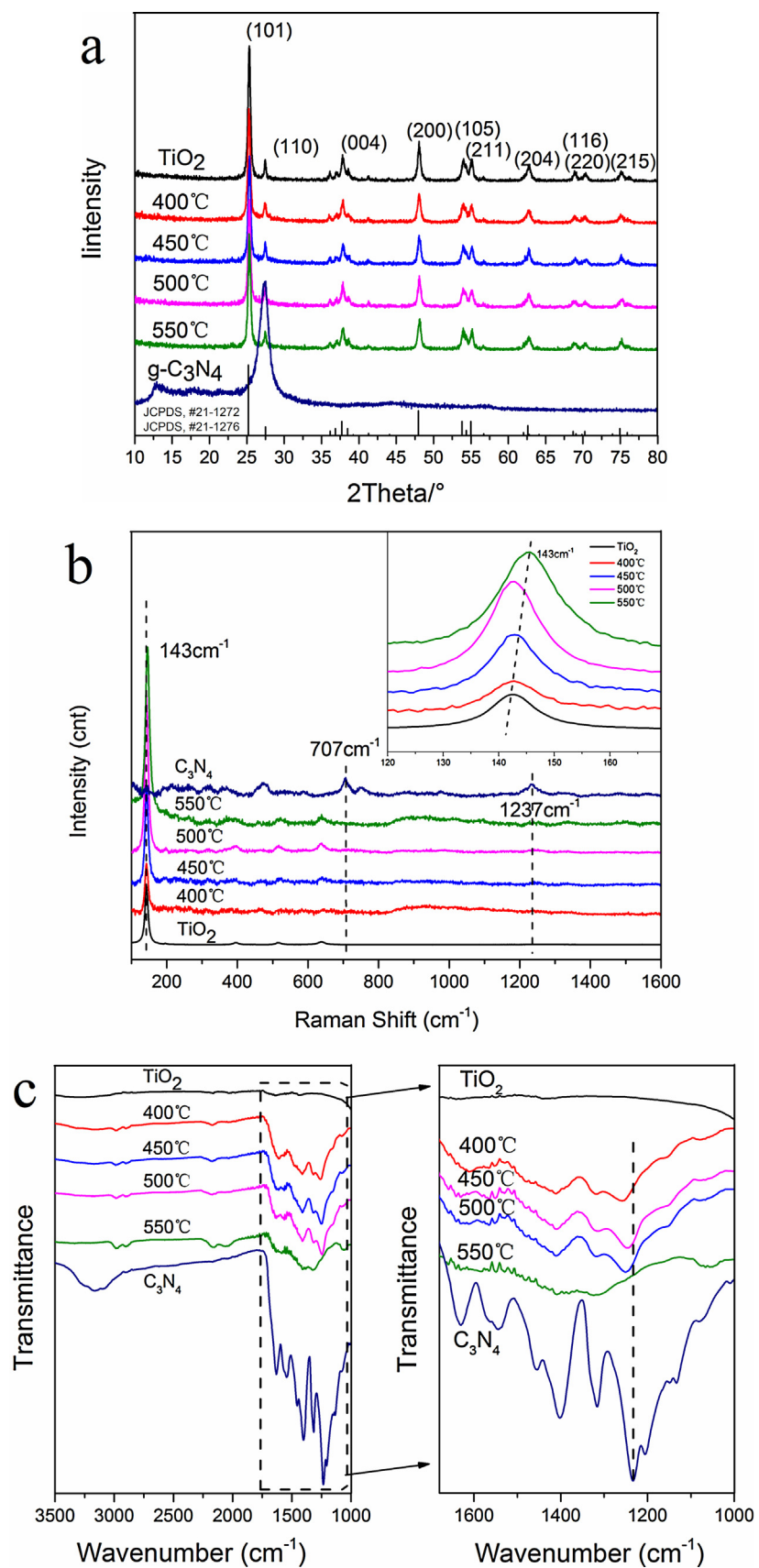


Fig. 2. (a) XRD patterns, (b) Raman spectra, (c) FT-IR spectra of g-C<sub>3</sub>N<sub>4</sub> and TiO<sub>2</sub> and g-C<sub>3</sub>N<sub>4</sub>@TiO<sub>2</sub> core-shell photocatalysts annealed at temperature of 400, 450, 500, 550 °C.

$\text{N}_2$  protection for 4 h. All of the  $\text{g-C}_3\text{N}_4@\text{TiO}_2$  sample are uniformly core-shell structure, seen in Fig. S1.

As can be seen in Fig. 1, the measured lattice spacing on the crystal is 0.351 nm, which corresponds to the anatase  $\text{TiO}_2$  (101) plane. The lattice structure of  $\text{TiO}_2$  is very orderly, and the outer  $\text{g-C}_3\text{N}_4$  layer of as-fabricated sample is significantly different from  $\text{TiO}_2$  core. A distinct core-shell structure is formed and the different layers of  $\text{g-C}_3\text{N}_4$  coated on the outer surface of  $\text{TiO}_2$  nanostructure material are approximately 1.0 nm, 1.5 nm and 3.0 nm (Fig. 1b–d), respectively assigned to the  $\text{g-C}_3\text{N}_4@\text{TiO}_2$  core-shell photocatalyst prepared at annealing temperature 550 °C, 500 °C and 400 °C. As contrast experiment, 0.0 nm  $\text{g-C}_3\text{N}_4@\text{TiO}_2$  sample is prepared by pure  $\text{TiO}_2$  annealed at 550 °C (Fig. 1a). Additionally, as shown in Fig. S1 e and f, the irregular morphology of the  $\text{g-C}_3\text{N}_4$  sol layer are coated on the outer surface of  $\text{TiO}_2$  particles. All of homogeneous  $\text{g-C}_3\text{N}_4@\text{TiO}_2$  core-shell structure samples are observed without existence of discrete  $\text{g-C}_3\text{N}_4$  phase, as can be seen in Fig. S1 a, b, c and d. The core-shell structure could be formed under wide temperature region between 400 °C to 550 °C. And the thickness of the  $\text{g-C}_3\text{N}_4$  shell is different with the increase of the annealing temperature, which is related to the assembly degree of CN sol on the surface of  $\text{TiO}_2$ . From the point of view on the catalyst color, the catalyst color gradually changes from light yellow to dark yellow as the annealing temperature increases from 400 °C to 550 °C leading to different light absorb abilities. The results show that controlled ultrathin  $\text{g-C}_3\text{N}_4$  layers depend on the assembly degree of CN precursors on the outer surface of  $\text{TiO}_2$ , and the assembly degree is the optimal when the samples annealed at the temperature of 550 °C.

The crystalline structures and phase purities are determined by XRD characterization, as shown in Fig. 2a. Characteristic diffraction peaks for the typical anatase  $\text{TiO}_2$  (JCPDS, #21-1272) are assigned to the (101), (004), (200), (105), (211), (204), (116), (220) and (215) planes, and the weak characteristic diffraction peaks for rutile  $\text{TiO}_2$  (JCPDS, #21-1276) is assigned to the (110) plane. And the strong peak at around 27.4° is assigned to (002) plane of  $\text{g-C}_3\text{N}_4$  crystal which is from the interplanar stacking of the aromatic system [37] and the broad one at 13.0° is assigned to (100) plane which is attributed to triazine repeat units [38]. The XRD pattern of as prepared  $\text{g-C}_3\text{N}_4@\text{TiO}_2$  samples show the typical peaks of anatase  $\text{TiO}_2$  and rutile  $\text{TiO}_2$ . There is no obvious change on the crystalline structures and phase purities after modification by  $\text{g-C}_3\text{N}_4$ , indicating that the process of calcination and re-assembled under high temperature does not influence the lattice structure of the  $\text{TiO}_2$  core. However, the characteristic peaks of bulk  $\text{g-C}_3\text{N}_4$  could not be observed on the composite photocatalysts. Because the shell thickness of 1.0 nanometers belongs to a short-range ordered structure, which is a normal phenomenon that the characteristic peaks of  $\text{g-C}_3\text{N}_4$  could not be observed on XRD figure of the composite photocatalysts. The interaction between the  $\text{TiO}_2$  core and the  $\text{g-C}_3\text{N}_4$  shell will be further confirmed by subsequent Raman technique and FT-IR spectra.

As shown in Fig. 2b, the Raman shift at 707  $\text{cm}^{-1}$  arises from the breathing modes of the s-triazine ring in  $\text{g-C}_3\text{N}_4$  [39]. The Raman shift at 1237  $\text{cm}^{-1}$  is associated with the lattice vibration of  $\text{g-C}_3\text{N}_4$  crystal. And the typical Raman shift at 143  $\text{cm}^{-1}$  is assigned to the lattice vibration of  $\text{TiO}_2$  crystal. Typical Raman peaks of  $\text{TiO}_2$  at 143  $\text{cm}^{-1}$  shows in the  $\text{g-C}_3\text{N}_4@\text{TiO}_2$  samples, however these Raman peaks of  $\text{g-C}_3\text{N}_4$  could not be seen clearly in the composite samples since the response signal of  $\text{TiO}_2$  is very strong. However, the Raman peak at 143  $\text{cm}^{-1}$  shows apparent redshift and this large degree of Raman shift is caused by the formation of new chemical bond at the interface between  $\text{g-C}_3\text{N}_4$  and  $\text{TiO}_2$  indicating the successful formation of  $\text{g-C}_3\text{N}_4@\text{TiO}_2$  core-shell structure. The interaction between the core and the shell can be further confirmed by FT-IR spectra, as shown in Fig. 2c. The characteristic bands at the range of 1100–1600  $\text{cm}^{-1}$  are attributed to the stretching vibra-

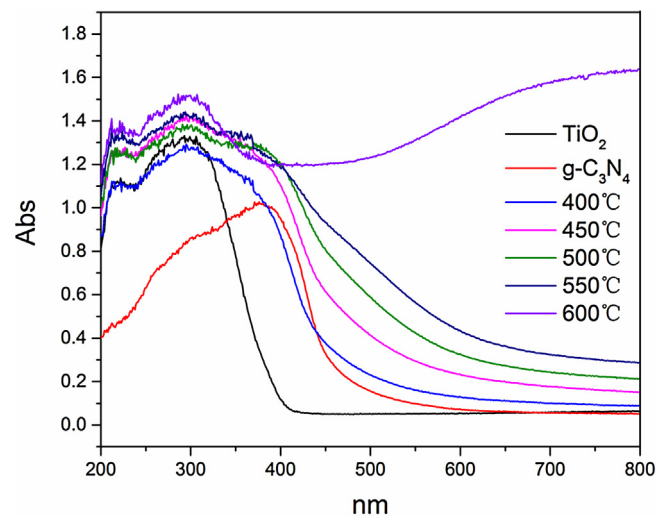


**Fig. 3.** Diffuse reflectance absorption spectra of  $\text{g-C}_3\text{N}_4$  and  $\text{TiO}_2$  and  $\text{g-C}_3\text{N}_4@\text{TiO}_2$  core-shell photocatalysts annealed at the temperature of 400, 450, 500, 550 °C, 600 °C.

tion of aromatic C–N heterocycle in bulk  $\text{g-C}_3\text{N}_4$ , which indicates the well development of polymeric melon network in composite samples [40]. The peaks of bulk  $\text{g-C}_3\text{N}_4$  in composite samples are obviously redshift with the increase of annealing temperature, since the new bonds of  $\text{g-C}_3\text{N}_4@\text{TiO}_2$  interface lead to a decline for the long-range ordered arrangement of ultrathin  $\text{g-C}_3\text{N}_4$  layer and the conjugation network structure is also slightly reduced.

The optical properties are evaluated by UV-vis diffuse reflectance spectra, which is shown in Fig. 3. As expected, all of the  $\text{g-C}_3\text{N}_4@\text{TiO}_2$  sample broaden the spectral response range so as to make use of visible light, while the absorption edge of  $\text{g-C}_3\text{N}_4@\text{TiO}_2$  exhibits an apparent redshift compared with bulk  $\text{g-C}_3\text{N}_4$  and pure  $\text{TiO}_2$ . And the absorption edge of  $\text{g-C}_3\text{N}_4@\text{TiO}_2$  obtained under 550 °C is the widest and the absorption intensity of the sample is the optimal. While  $\text{g-C}_3\text{N}_4@\text{TiO}_2$  annealed at 600 °C shows a strong absorption area in visible and infrared range, which indicates the surface area and phase transformation occurred during the annealing process. So the surface area and phase transformation are also accounted for the poor photocatalytic performance.

### 3.2. Photocatalytic activity and photocurrent response

The degradation of phenol and photocurrent response test under visible light and UV light spectra were evaluated to reveal the photocatalytic activity of  $\text{g-C}_3\text{N}_4@\text{TiO}_2$  core-shell catalyst. As shown in Fig. 4a, the photocatalytic activity in degradation phenol of  $\text{g-C}_3\text{N}_4@\text{TiO}_2$  core-shell photocatalyst under visible light irradiation is much higher than that of pure  $\text{TiO}_2$ , bulk  $\text{g-C}_3\text{N}_4$  and physical mixture  $\text{g-C}_3\text{N}_4@\text{TiO}_2$ . With the annealing temperature increasing, the degradation activity of  $\text{g-C}_3\text{N}_4@\text{TiO}_2$  photocatalyst is gradually enhanced, which shows an order of 550 > 500 > 450 > 400 > 600 °C. Especially the degradation activity of  $\text{g-C}_3\text{N}_4@\text{TiO}_2$  annealed at 550 °C Exhibits 7.2 times higher than that of bulk  $\text{g-C}_3\text{N}_4$ . The result shows that CN sol precursor has the optimal degree of re-assembled on the surface of  $\text{TiO}_2$  when the annealing temperature is 550 °C. While  $\text{g-C}_3\text{N}_4@\text{TiO}_2$  annealed at 600 °C shows the worst photo-degradation phenol performance in all core-shell structures owing to carbonization phenomenon which is the catalyst becomes black powder. As shown in Fig. 4b, the degradation phenol activity under ultraviolet light can be regulated according to the content of  $\text{g-C}_3\text{N}_4$  in  $\text{g-C}_3\text{N}_4@\text{TiO}_2$  sample. When the content of  $\text{g-C}_3\text{N}_4$  are 0.2 wt%, 0.6 wt% and 1 wt%, the reaction rate constants of degradation phenol are 1.05, 1.15, 1.11 times higher than

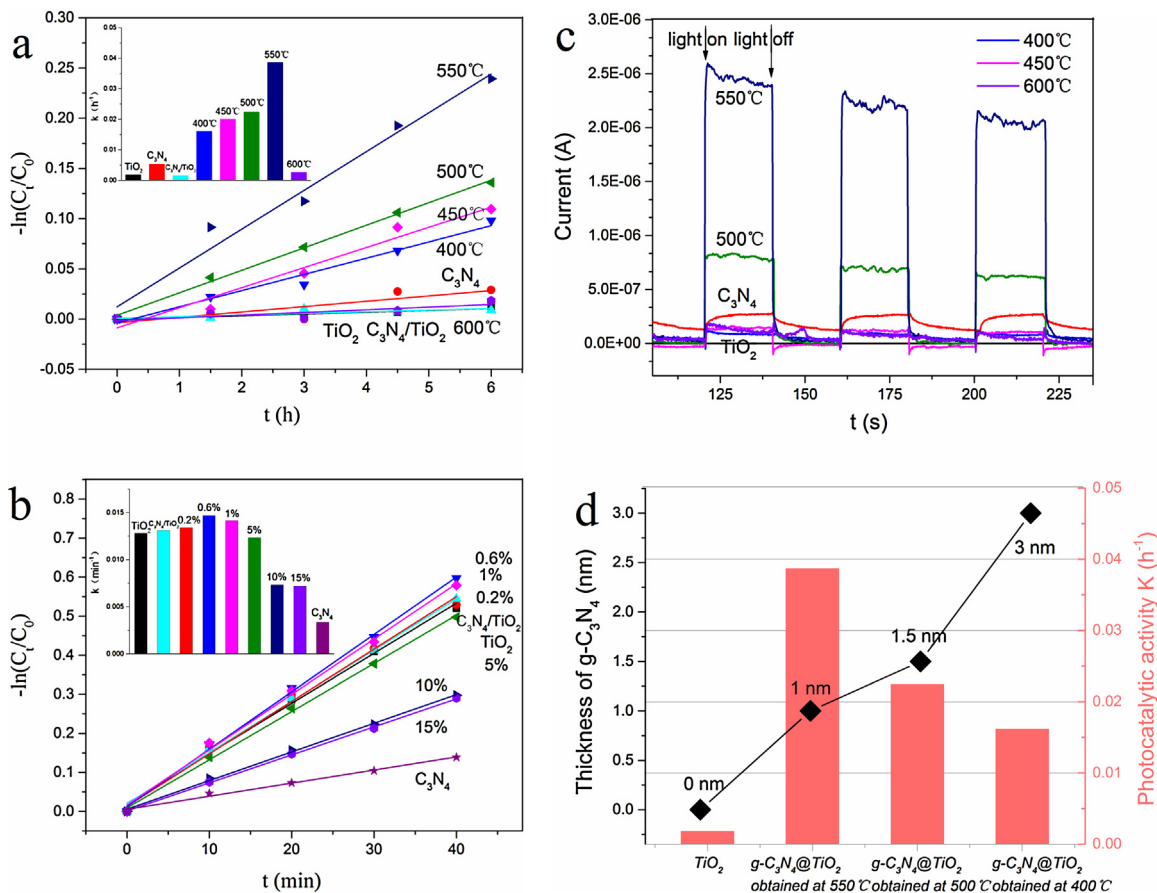


**Fig. 4.** Photocatalytic activity of phenol over  $\text{g-C}_3\text{N}_4@\text{TiO}_2$  core-shell photocatalyst and physical mixture  $\text{g-C}_3\text{N}_4/\text{TiO}_2$  (a) visible light ( $\lambda_{\text{vis}} \geq 450 \text{ nm}$ ), (b) UV light ( $\lambda = 254 \text{ nm}$ ), (c) the transient photocurrent density responses of  $\text{g-C}_3\text{N}_4@\text{TiO}_2$  core-shell photocatalyst and (d) the relationship between layer thickness of  $\text{g-C}_3\text{N}_4$  shell and photocatalytic activity under visible light ( $\lambda_{\text{vis}} \geq 450 \text{ nm}$ ).

that of pure  $\text{TiO}_2$ , respectively. And the degradation phenol activity using these samples are also higher than that of physical mixture  $\text{g-C}_3\text{N}_4/\text{TiO}_2$ . While with the content of  $\text{g-C}_3\text{N}_4$  further increase, the reaction rate of degradation phenol dramatically declines because the thickness of the  $\text{g-C}_3\text{N}_4$  shell affects the absorption capacity of  $\text{TiO}_2$  under ultraviolet light. As shown in Fig. S3, the catalytic activity of low content of  $\text{g-C}_3\text{N}_4$  core-shell structure catalyst under full spectrum has no apparent decreased compared with that of pure material. The law of the absorption capacity of  $\text{TiO}_2$  under full spectrum is consistent with that of ultraviolet light. The results show that  $\text{g-C}_3\text{N}_4@\text{TiO}_2$  core-shell structure photocatalyst exhibits excellent activity in the visible region which counts for 47% of the sunlight. Thus the material has obvious advantages in the catalytic degradation under sunlight.

As shown in Fig. 4c, photocurrent of  $\text{g-C}_3\text{N}_4@\text{TiO}_2$  electrodes increase remarkably with the annealing temperature rise from  $400^\circ\text{C}$  to  $500^\circ\text{C}$ , showing an order of samples at  $550 > 500 > 450 > 400 > 600^\circ\text{C}$ . The sample of  $\text{g-C}_3\text{N}_4@\text{TiO}_2$  obtained at  $550^\circ\text{C}$  exhibits the highest photocurrent response intensity, which is increased by ten times higher than that of  $\text{g-C}_3\text{N}_4$  and five orders of magnitude compare to  $\text{TiO}_2$ . While the sample obtained at  $600^\circ\text{C}$  shows the worst performance, which is in well accordance with photo-degradation of phenol performance. The increase of photocurrent indicates that there may exist chemical bond between  $\text{g-C}_3\text{N}_4$  shell and  $\text{TiO}_2$  core, which can enhance the separation efficiency of photogenerated carriers leading to a greatly improvement of the visible light photocatalytic activity.

The structure-activity relationship was profoundly revealed by accurately matching between controlled ultrathin  $\text{g-C}_3\text{N}_4$  layer of

$\text{g-C}_3\text{N}_4@\text{TiO}_2$  sample and the corresponding photo-degradation phenol activity, shown in Fig. 4d. As contrast experiment, 0 nm  $\text{g-C}_3\text{N}_4@\text{TiO}_2$  sample is prepared by pure  $\text{TiO}_2$  annealed at  $550^\circ\text{C}$ . The different layers of  $\text{g-C}_3\text{N}_4$  over  $\text{g-C}_3\text{N}_4@\text{TiO}_2$  sample are 1.0 nm, 1.5 nm and 3.0 nm prepared at annealing temperature  $550^\circ\text{C}$ ,  $500^\circ\text{C}$  and  $400^\circ\text{C}$ , respectively. With the annealing temperature increasing, the thickness of  $\text{g-C}_3\text{N}_4$  layer gradually reduces. Accordingly, the reaction rate constants of photo-degradation phenol activity are  $0.0018 \text{ h}^{-1}$ ,  $0.0386 \text{ h}^{-1}$ ,  $0.0224 \text{ h}^{-1}$  and  $0.0161 \text{ h}^{-1}$ . With the increase of the  $\text{g-C}_3\text{N}_4$  layer from 0 nm to 1.0 nm, the reaction rate constant gradually enhances from  $0.0018 \text{ h}^{-1}$  to  $0.0386 \text{ h}^{-1}$ . While if further increasing the  $\text{g-C}_3\text{N}_4$  layer, the reaction rate constant decline. So the optimal catalytic activity is achieved by the thickness of 1.0 nm  $\text{g-C}_3\text{N}_4$  layer. Because with the increase of the thickness of  $\text{g-C}_3\text{N}_4$  layer in a certain range from 0 nm to 1.0 nm, it is conducive to enhance the absorption ability of visible light for the  $\text{g-C}_3\text{N}_4@\text{TiO}_2$  core-shell photocatalyst. When the thickness of  $\text{g-C}_3\text{N}_4$  layer are 1.5 nm and 3.0 nm, the super-abundant  $\text{g-C}_3\text{N}_4$  layer seriously hinders the electron transfer from  $\text{g-C}_3\text{N}_4$  to  $\text{TiO}_2$ , leading to the decrease of photocatalytic activity. The trend of layer-dependent effect over degradation phenol under visible light ( $\lambda_{\text{vis}} \geq 450 \text{ nm}$ ) is consistent with that of visible light ( $\lambda_{\text{vis}} \geq 420 \text{ nm}$ ), shown in Fig. S2 (a) and (b). The rule of layer-dependent effect can provide the basis for the design of other organic-inorganic core-shell structure photocatalytic system.

Total organic carbon analyzer (TOC) was used to evaluate the degree of mineralization of the  $\text{g-C}_3\text{N}_4@\text{TiO}_2$  photocatalyst obtained at  $550^\circ\text{C}$  under optimized experimental conditions for phenol. Fig. 5a shows the results for the degradation and min-

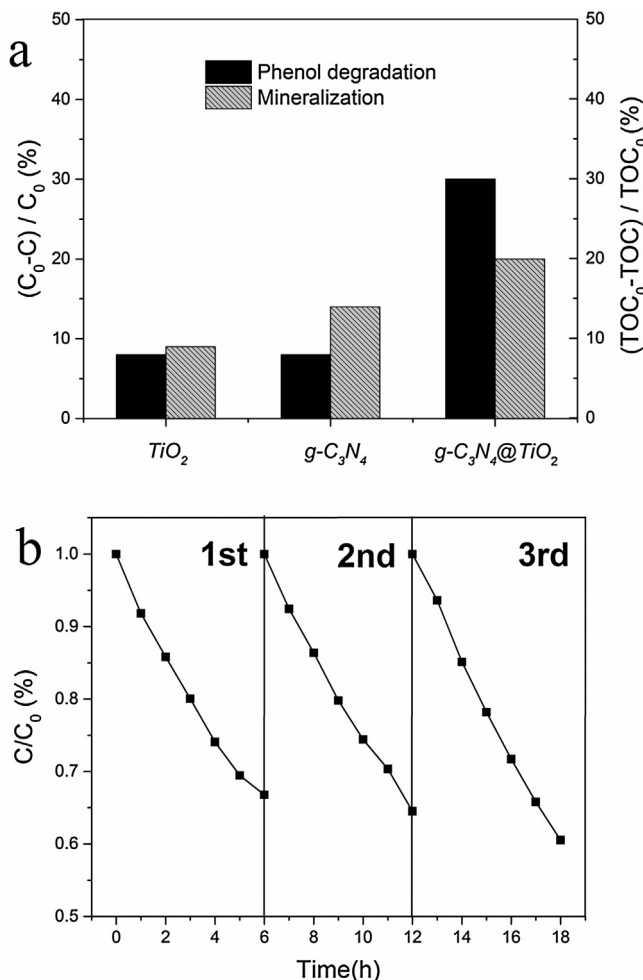


**Fig. 5.** (a) Degradation content and mineralization of phenol under visible light irradiation ( $\lambda_{vis} \geq 420$  nm) and (b) recycle experiment over  $g-C_3N_4@TiO_2$  photocatalyst obtained at 550 °C.

eralization of phenol under visible light irradiation after 6 h. The removal rate of phenol using  $g-C_3N_4@TiO_2$  core-shell catalyst is 30% and the degree of mineralization by the same catalyst is 19.8%, which dramatically increase compared with that of  $g-C_3N_4$  and  $TiO_2$  indicating the core-shell structure material can not only improve the degradation rate of phenol but also significantly improve the capability of mineralization. The enhancement of the mineralization ability can attribute to the formation of  $g-C_3N_4@TiO_2$  core-shell structure, which could decline the valence band of the  $g-C_3N_4$ . Detailed explanation for the results will be given in density functional theory calculation subsequently.

In order to detect the stability of  $g-C_3N_4@TiO_2$  core-shell structure catalyst, the cyclic parallel test of photocatalytic degradation of phenol is carried out in this study. As shown in Fig. 5b, the removal degree of phenol in the three-round continuous reaction test using  $g-C_3N_4@TiO_2$  core-shell catalyst are 33.2%, 35.5% and 39.5%, which indicates the core-shell structure material is stable during the three-round photo-degradation process. The results of cycle experiment show that the  $g-C_3N_4@TiO_2$  prepared by the sol-gel method has a strong binding force between the core and shell, which effectively reduces the dissolution of bulk  $g-C_3N_4$  material during the photocatalytic process and convenient for recycling. Moreover, compared with the first round, the catalytic activity during the latter two rounds of experiments do not decline, due to the  $g-C_3N_4@TiO_2$  core-shell structure catalyst can be recycled completely without lost in the process of centrifugal separation.

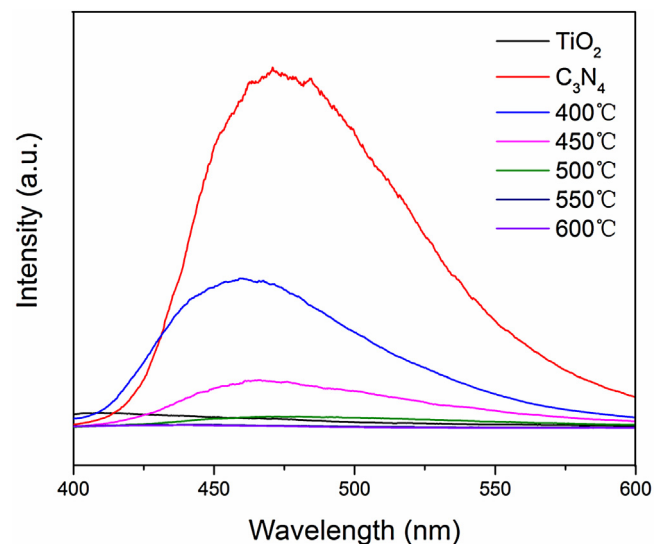


**Fig. 6.** Photoluminescence spectra of  $g-C_3N_4$ ,  $TiO_2$  and  $g-C_3N_4@TiO_2$  core-shell photocatalysts annealed at temperature of 400, 450, 500, 550, 600 °C.

The reproducibility of  $g-C_3N_4@TiO_2$  core-shell catalysts fabricated by CN sol-gel process is investigated, the different three samples with the best degradation activity under visible light irradiation are used in this experiment for degradation of phenol. As shown in Fig. S4, CN solids are heated at reflux in a concentrated  $HNO_3$  solution at 80 °C to produce a stable CN colloidal solution, which can be re-established the conjugation systems on the surface of  $TiO_2$  through removal of  $HNO_3$  by direct heating above 400 °C. The result suggests that the new method to prepare  $g-C_3N_4@TiO_2$  core-shell structure catalyst with controlled ultrathin  $g-C_3N_4$  layer has well reproducibility.

### 3.3. Mechanism of photocatalytic activity enhancement

#### 3.3.1. Photoluminescence spectra

The photoluminescence technique is used to investigate the separation, transfer and recombination processes of photogenerated carriers in  $g-C_3N_4@TiO_2$  core-shell photocatalyst. As shown in Fig. 6, bulk  $g-C_3N_4$  exhibits a strong broad range (430–550 nm) and peaks at 470 nm in the photoluminescence spectrum, which is mainly caused by the recombination of photogenerated electrons and holes produced by  $g-C_3N_4$  material [41]. While the peaks of the core-shell photocatalyst decrease remarkably, indicating that the fluorescence can be highly quenched when introducing a specific core-shell structure. It could be deduced from the above results of photoluminescence spectrum that photogenerated charges are highly stabilized at the interfaces of the  $g-C_3N_4@TiO_2$  core-shell structure, so their recombination rate is greatly reduced. In addition, with the annealing temperature increasing, the photoluminescence intensity gradually decline, indicating that ultrathin  $g-C_3N_4$  layer can efficiently promote the separation of photogenerated carriers which is important for their utilization in photocatalytical chemistry. This regulation is consistent with that of the photoelectric properties as shown in Fig. 4c, which demonstrates that the  $g-C_3N_4@TiO_2$  core-shell structure catalyst prepared by sol-gel solution and *in situ* re-assembled process can effectively enhance the activity of phenol degradation.

#### 3.3.2. Calculation investigation

Fig. 7(a) and (b) gave the atomic model of bulk  $TiO_2$  and  $g-C_3N_4$  structure. According to the experimental HRTEM observation of fringer print of the interface contact planes, it would be insightful to construct a theoretical heterojunction model through contact-

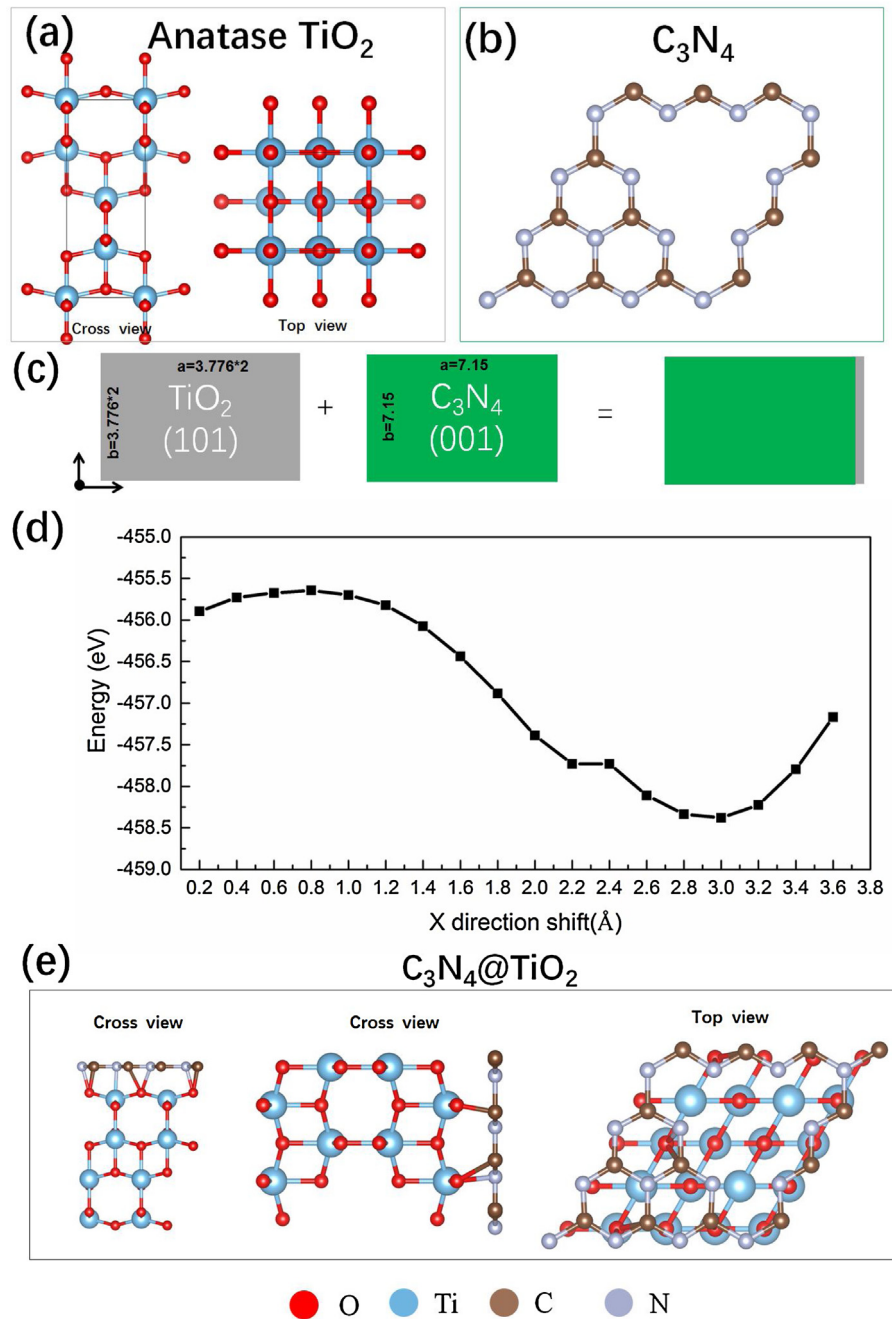


**Fig. 7.** (color online) (a) side top view of anatase  $\text{TiO}_2$ , (b) top view of  $\text{C}_3\text{N}_4$  and (c) Schematic construction of the interface between anatase  $\text{TiO}_2$  and  $\text{C}_3\text{N}_4$ . (d) Finally built configuration of heterojunction  $\text{TiO}_2/\text{C}_3\text{N}_4$ .

ing  $\text{TiO}_2$  (101) plane and  $\text{g-C}_3\text{N}_4$  (001) plane. What's more, the (101) crystal planes of  $\text{TiO}_2$  and (001) crystal planes of  $\text{g-C}_3\text{N}_4$  were selected owing to a small planar mismatch between these two planes. Fig. 7(c) depicts construction process of the interface between  $\text{TiO}_2$  and  $\text{g-C}_3\text{N}_4$ . In order to minimize this effect of local structure relaxation since that DFT could optimize structure locally rather than globally,  $\text{TiO}_2$  is shifted along x-direction from 0  $\text{\AA}$  to 3.6  $\text{\AA}$  prior to a structural relaxation of the interface. When the X axis shift to 3.0  $\text{\AA}$ , total energy is the lowest in all shift process shown in Fig. 7(d). Subsequently, based on the x axis shift-determined optimized structure, a fully structure relaxation is performed. As a result, the interface configuration of  $\text{TiO}_2@\text{g-C}_3\text{N}_4$  is obtained shown in Fig. 7(e). At the interface  $\text{TiO}_2/\text{g-C}_3\text{N}_4$ , oxygen atoms are bonded with N or C atoms with the N–O bond length

1.74  $\text{\AA}$  and C–O bond length 1.83  $\text{\AA}$ . Each interfacial oxygen atom bonds to one C in the upper  $\text{C}_3\text{N}_4$  region and one Ti atom in  $\text{TiO}_2$  region. In order to further explore interfacial bonding information, bond angles are calculated. Interfacial Ti–O–C angle is 106°. Resulting from the strong dissociation energy of O–Ti or O–C bond and small planar strain, the corresponding interfacial model is a realistic reflection of interfacial bonding situations (Fig. 8).

The electrostatic potential of pure anatase  $\text{TiO}_2$ ,  $\text{g-C}_3\text{N}_4$  and  $\text{TiO}_2/\text{g-C}_3\text{N}_4$  with coating layers changing from 1–3, to 5 were shown in Fig. 7. The workfunction of anatase  $\text{TiO}_2$  and  $\text{g-C}_3\text{N}_4$  is 5.67 eV and 4.82 eV, respectively, meaning that electrons which transfer from surface to infinite needs more energy for anatase  $\text{TiO}_2$ . For the interface  $\text{TiO}_2/\text{g-C}_3\text{N}_4$  with one layer  $\text{g-C}_3\text{N}_4$ , the electrostatic potential of  $\text{TiO}_2$  is bigger than that of  $\text{g-C}_3\text{N}_4$ , ~3.87 eV.

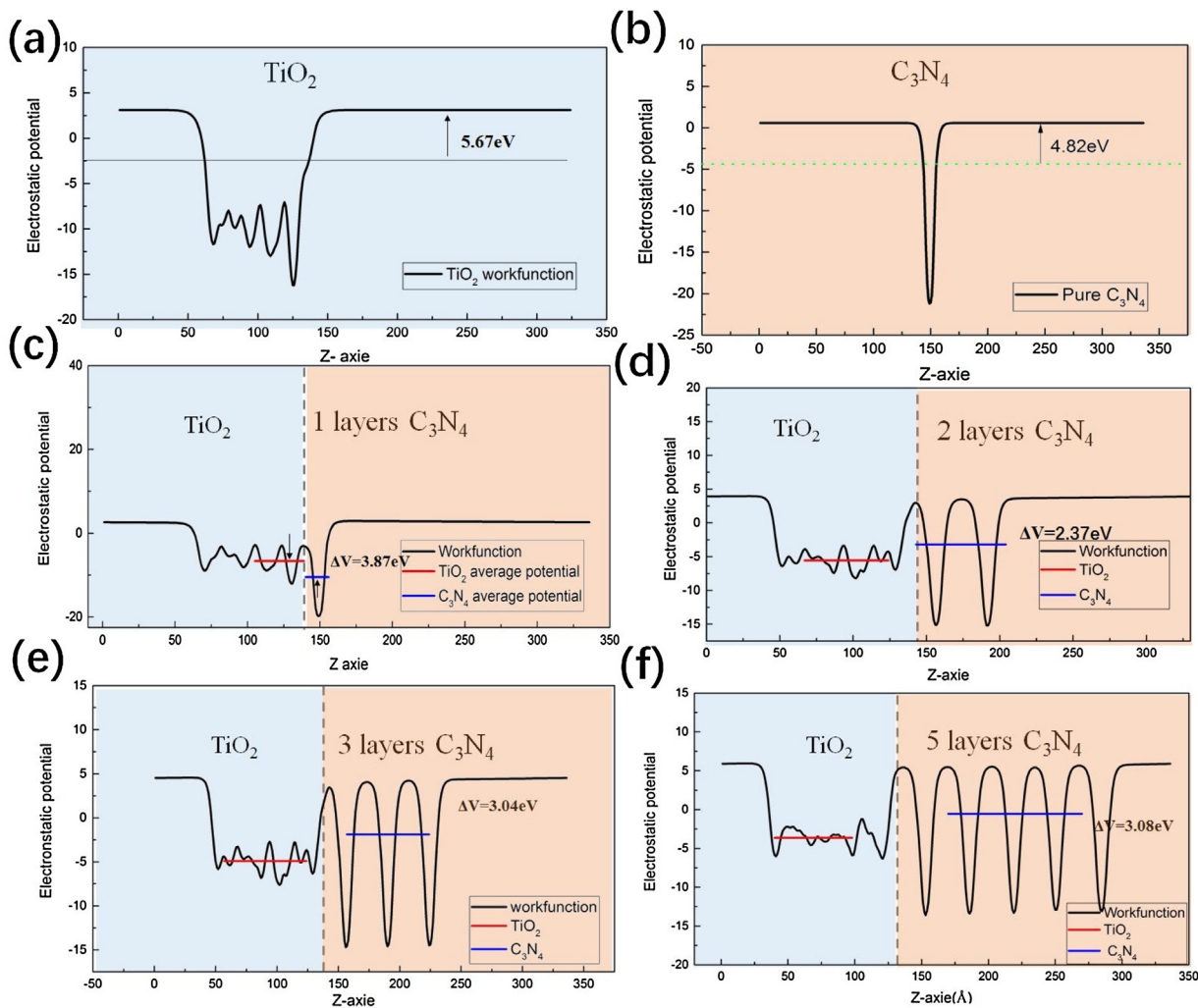


**Fig. 8.** Induced change in the electrostatic potential by the interface formation,  $\Delta V = V - V_{C_3N_4} - V_{TiO_2}$  the electrostatic potential for TiO<sub>2</sub> (a), C<sub>3</sub>N<sub>4</sub> (b), TiO<sub>2</sub>@C<sub>3</sub>N<sub>4</sub> with 1(c), 2(d), 3(e), 5(f) layers.

While, the electrostatic potential of TiO<sub>2</sub> is lower than that of g-C<sub>3</sub>N<sub>4</sub> for the interface TiO<sub>2</sub>/g-C<sub>3</sub>N<sub>4</sub> with 2,3,5 layers g-C<sub>3</sub>N<sub>4</sub>. What's more, the electrostatic potential difference of g-C<sub>3</sub>N<sub>4</sub> to TiO<sub>2</sub> is increasing from 2.37 eV, 3.04 eV to 3.08 eV. We drew a trend of electrostatic potential difference with g-C<sub>3</sub>N<sub>4</sub> layers and showed in Fig. 9. The trend is consistent with photo-degradation phenol activity in our experiment (seen in Fig. 4d).

### 3.3.3. Photocatalytic mechanism

To further elucidate the mechanism of photocatalytic degradation activity enhancement, the interface charge separation efficiency is investigated by the electrochemical impedance spectroscopy (EIS). As shown in Fig. S5, the arc radius of EIS measured at high frequencies over bulk g-C<sub>3</sub>N<sub>4</sub>, pure TiO<sub>2</sub> and g-C<sub>3</sub>N<sub>4</sub>@TiO<sub>2</sub> samples indicate corresponding resistance of the equivalent circuit components of electrochemical system which reflects the separation rate of photogenerated carriers and the efficiency of charge transfer across the electrode-electrolyte interface. The arc radius of EIS by g-C<sub>3</sub>N<sub>4</sub>@TiO<sub>2</sub> sample is smaller than that of pure TiO<sub>2</sub> and bulk g-C<sub>3</sub>N<sub>4</sub>. Accordingly, resistance of the equivalent circuit components fitted by g-C<sub>3</sub>N<sub>4</sub>@TiO<sub>2</sub> sample with and without light irradiation are 5.22E10 ohm and 2.17E05 ohm, which exhibits that g-C<sub>3</sub>N<sub>4</sub>@TiO<sub>2</sub> photocatalyst obtained at 550 °C has excellent photo-performance. Resistance of the equivalent circuit components of pure TiO<sub>2</sub> and bulk g-C<sub>3</sub>N<sub>4</sub> without light irradiation (4.55E11 ohm

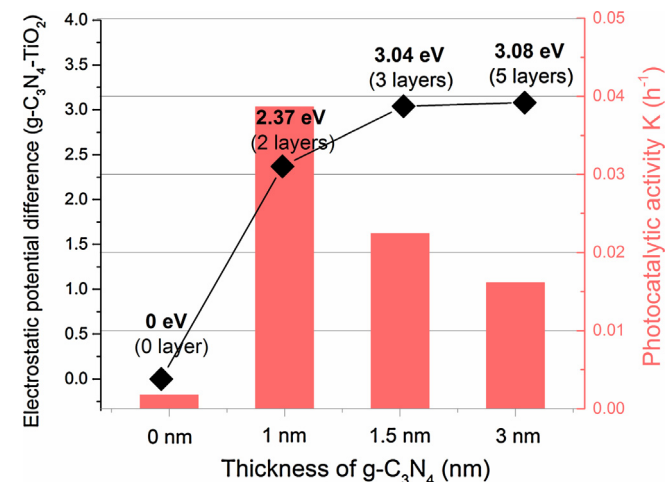


**Fig. 9.** The relationship between electrostatic potential difference, photocatalytic activity and thickness of g-C<sub>3</sub>N<sub>4</sub>.

and 9.28E11 ohm, respectively) and under visible light irradiation (3.19E11 ohm and 2.53E11 ohm, respectively) are both higher than those of g-C<sub>3</sub>N<sub>4</sub>@TiO<sub>2</sub> sample, which reveals that the core-shell

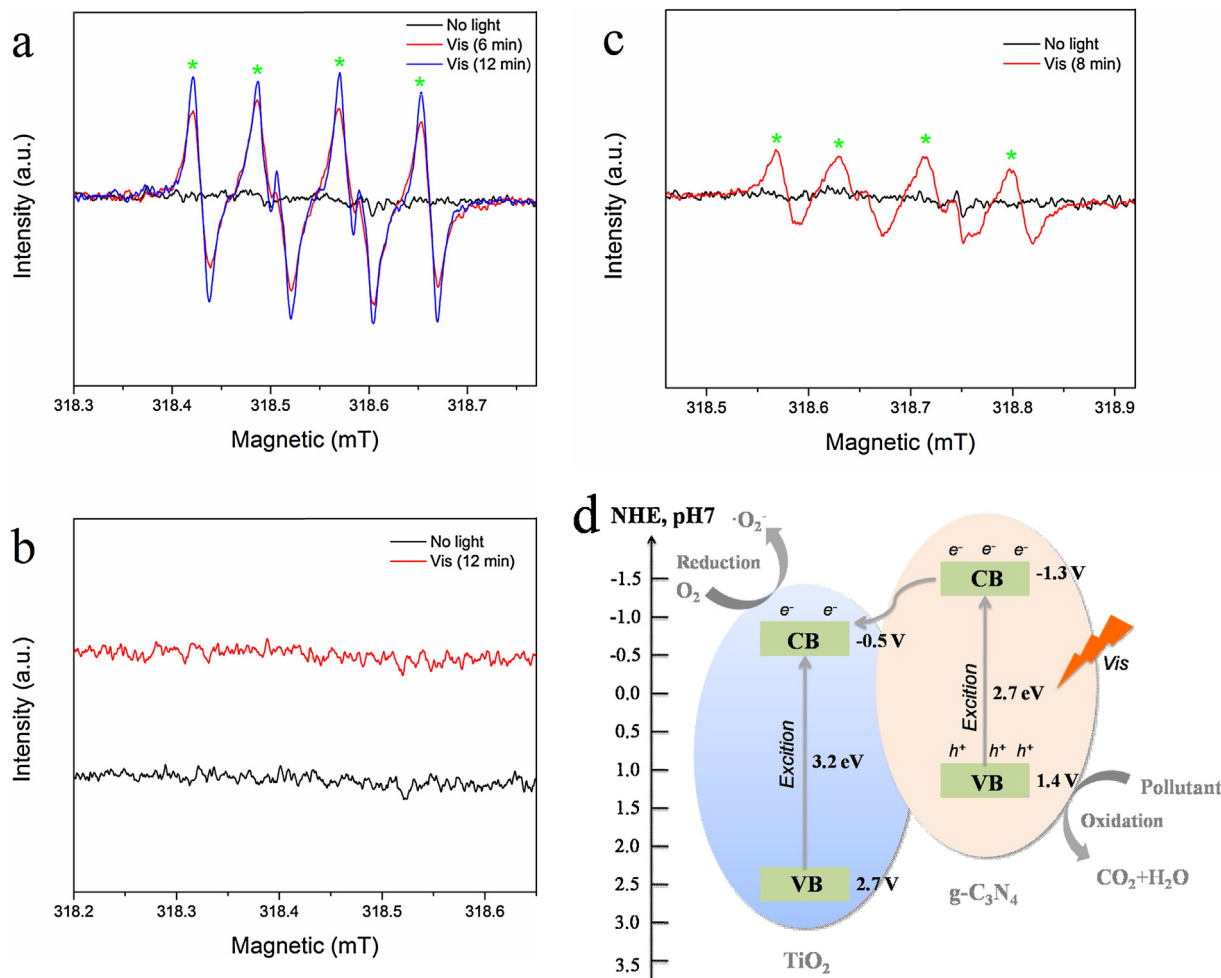


**Fig. 10.** Electron spin resonance spectroscopy of  $\text{g-C}_3\text{N}_4@\text{TiO}_2$  core-shell photocatalyst without and with visible light irradiation ( $\lambda_{\text{Vis}} \geq 420 \text{ nm}$ ) (a) Superoxide radical test in methanol solvents with DMPO (50 mM) as radical trapper and (b) Hydroxyl radical test in aqueous solvents with DMPO (50 mM) as radical trapper and (c) Superoxide radical test in methanol solvents with DMPO (50 mM) as radical trapper using  $\text{g-C}_3\text{N}_4$  and (d) schematic illustration of electron hole separation over  $\text{g-C}_3\text{N}_4@\text{TiO}_2$  core-shell photocatalyst under visible light irradiation.

structure promotes the efficient transfer of photogenerated carriers resulting enhancement of the photocatalytic activity.

Electron spin resonance spectroscopy (ESR) of  $\text{g-C}_3\text{N}_4@\text{TiO}_2$  core-shell photocatalyst without and with visible light irradiation is shown in Fig. 10. It is necessary to detect the main oxidative species in photocatalytic degradation process for elucidating the photocatalytic mechanism. As seen in Fig. 10a, there is no obvious peak in the absence of light irradiation. Under the visible light, the ESR signal of  $\text{g-C}_3\text{N}_4@\text{TiO}_2$  core-shell structure material exhibits obvious superoxide ( $\cdot\text{O}_2$ ) crack peak, indicating that the methanol solution of  $\text{g-C}_3\text{N}_4@\text{TiO}_2$  core-shell structure material can produce  $\cdot\text{O}_2$  which is likely to be one of the main active species of the photocatalytic reaction. As seen in Fig. 10b, there is no signal in the dark and also under visible light irradiation. The result means hydroxyl radicals ( $\cdot\text{OH}$ ) are probably not the active species during photocatalytic reaction. As shown in Fig. 10c, the ESR signal of  $\text{g-C}_3\text{N}_4$  exhibits obvious superoxide ( $\cdot\text{O}_2$ ) crack peak under the visible light, indicating that the methanol solution of  $\text{g-C}_3\text{N}_4$  can produce  $\cdot\text{O}_2$ . On the basis of the above analysis, a possible mechanism for the phenol degradation over  $\text{g-C}_3\text{N}_4@\text{TiO}_2$  core-shell photocatalyst under visible irradiation is proposed as shown in Fig. 10d. Photogenerated electrons and holes are generated on CB and VB of  $\text{g-C}_3\text{N}_4$  shell under visible irradiation. The CB of  $\text{TiO}_2$  core is lower than that of  $\text{g-C}_3\text{N}_4$  shell, so the photogenerated electrons can be injected easily from  $\text{g-C}_3\text{N}_4$  into the  $\text{TiO}_2$  core. When  $\text{O}_2$  gas encounters the

electrons of  $\text{TiO}_2$  to generate  $\cdot\text{O}_2$ , both  $\cdot\text{O}_2$  and the holes on the VB of  $\text{g-C}_3\text{N}_4$  shows strong oxide capability, which contributes to the enhancement on phenol degradation activity of  $\text{g-C}_3\text{N}_4@\text{TiO}_2$  core-shell photocatalyst under visible light.

#### 4. Conclusion

The  $\text{g-C}_3\text{N}_4@\text{TiO}_2$  core-shell structure photocatalysts with controlled ultrathin  $\text{g-C}_3\text{N}_4$  layer are successfully fabricated by the new method of the sol-gel approaches *in situ* coating re-assembled, which profoundly reveals the structure-activity relationship between core-shell structure and photocatalytic activity. The  $\text{g-C}_3\text{N}_4@\text{TiO}_2$  sample with 1.0 nm thickness of shell layers has the highest visible light photocatalytic activity which is almost 7.2 times as high as that of bulk  $\text{g-C}_3\text{N}_4$ . The core-shell structure material can not only improve the degradation rate of phenol but also significantly improve the capability of mineralization. Moreover, the  $\text{g-C}_3\text{N}_4@\text{TiO}_2$  prepared by the sol-gel method has a strong binding force between the core and shell, which effectively reduces the dissolution of bulk  $\text{g-C}_3\text{N}_4$  material during the photocatalytic process and convenient for recovery. A new catalytic concept namely layer-dependent effect is found which can provide the basis for the design of other organic-inorganic core-shell structure photocatalytic system.

## Acknowledgements

This work was partly supported by National Basic Research Program of China (973 Program) (2013CB632403) and Chinese National Science Foundation (21437003, 21673126, 21621003, 51651201) and Collaborative Innovation Center for Regional Environmental Quality.

## Appendix A. Supplementary data

Supplementary data associated with this article can be found, in the online version, at <http://dx.doi.org/10.1016/j.apcatb.2017.08.004>.

## References

- [1] A. Fujishima, Nature 238 (1972) 37–38.
- [2] M. Wang, L. Cai, Y. Wang, F. Zhou, K. Xu, X. Tao, Y. Chai, J. Am. Chem. Soc. 139 (2017) 4144–4151.
- [3] D. Liu, J. Wang, X. Bai, R. Zong, Y. Zhu, Adv. Mater. 28 (2016) 7284–7290.
- [4] X. Wang, K. Maeda, A. Thomas, K. Takanabe, G. Xin, J.M. Carlsson, K. Domen, Nat. Mater. 8 (2009) 76–80.
- [5] J. Xu, L. Wang, Y. Zhu, Langmuir 28 (2012) 8418–8425.
- [6] J. Liu, Y. Liu, N. Liu, Y. Han, X. Zhang, H. Huang, Y. Lifshitz, S.T. Lee, J. Zhong, Z. Kang, Science 347 (2015) 970–974.
- [7] G. Zhang, S. Zang, X. Wang, ACS Catal. 5 (2015) 941–947.
- [8] R. Kuriki, K. Sekizawa, O. Ishitani, K. Maeda, Angew. Chem. Int. Ed. 54 (2015) 2406–2409.
- [9] M. Zhang, W. Yao, Y. Lv, X. Bai, Y. Liu, W. Jiang, Y. Zhu, J. Mater. Chem. A 2 (2014) 11432–11438.
- [10] M. Zhang, W. Luo, Z. Wei, W. Jiang, D. Liu, Y. Zhu, Appl. Catal. B-Environ. 194 (2016) 105–110.
- [11] Y. Zheng, L. Lin, B. Wang, X. Wang, Angew. Chem. Int. Ed. 54 (2015) 12868–12884.
- [12] M. Wen, Y. Cui, Y. Kuwahara, K. Mori, H. Yamashita, ACS Appl. Mater. Interfaces 8 (2016) 21278–21284.
- [13] M. Wen, K. Mori, Y. Kuwahara, H. Yamashita, ACS Energy Lett. 2 (2017) 1–7.
- [14] W. Jiang, W. Luo, R. Zong, W. Yao, Z. Li, Y. Zhu, Small 12 (2016) 4370–4378.
- [15] X. Bai, L. Wang, Y. Wang, W. Yao, Y. Zhu, Appl. Catal. B-Environ. 152–153 (2014) 262–270.
- [16] M. Zhang, W. Jiang, D. Liu, J. Wang, Y. Liu, Y. Zhu, Appl. Catal. B-Environ. 183 (2016) 263–268.
- [17] X.H. Li, X. Wang, M. Antonietti, Chem. Sci. 3 (2012) 2170–2174.
- [18] J. Sun, J. Zhang, M. Zhang, M. Antonietti, X. Fu, X. Wang, Nat. Commun. 3 (2012) 1139–1146.
- [19] D. Chen, K. Wang, T. Ren, H. Ding, Y. Zhu, Dalton Trans. 43 (2014) 13105–13114.
- [20] Z. Wei, F. Liang, Y. Liu, W. Luo, J. Wang, W. Yao, Y. Zhu, Appl. Catal. B-Environ. 201 (2017) 600–606.
- [21] K.N. Ferreira, T.M. Iverson, K. Maghlaoui, J. Barber, S. Iwata, Science 303 (2004) 1831–1838.
- [22] Y. Umena, K. Kawakami, J.R. Shen, N. Kamiya, Nature 473 (2011) 55–60.
- [23] G.S. Engel, T.R. Calhoun, E.L. Read, T.K. Ahn, T. Mancal, Y.C. Cheng, R.E. Blankenship, G.R. Fleming, Nature 446 (2007) 782–786.
- [24] X. Bai, R. Zong, C. Li, D. Liu, Y. Liu, Y. Zhu, Appl. Catal. B-Environ. 147 (2014) 82–91.
- [25] D. Chen, K. Wang, D. Xiang, R. Zong, W. Yao, Y. Zhu, Appl. Catal. B-Environ. 147 (2014) 554–561.
- [26] C. Pan, J. Xu, Y. Wang, D. Li, Y. Zhu, Adv. Funct. Mater. 22 (2012) 1518–1524.
- [27] Y. Wang, X. Bai, C. Pan, J. He, Y. Zhu, J. Mater. Chem. 22 (2012) 11568–11573.
- [28] J. Zhou, M. Zhang, Y. Zhu, Phys. Chem. Chem. Phys. 17 (2015) 3647–3652.
- [29] J. Zhou, M. Zhang, Y. Zhu, Phys. Chem. Chem. Phys. 16 (2014) 17627–17633.
- [30] J. Zhou, M. Zhang, L. Lin, X. Wang, Angew. Chem. Int. Ed. 54 (2015) 6297–6301.
- [31] J.P. Perdew, K. Burke, M. Ernzerhof, Phys. Rev. Lett. 77 (1996) 3865.
- [32] G. Kresse, J. Furthmüller, Comp. Mater. Sci. 6 (1996) 15.
- [33] G. Kresse, J. Furthmüller, Phys. Rev. B 54 (1996) 11169.
- [34] P.E. Blöchl, Phys. Rev. B 50 (1994) 17953.
- [35] W. Press, B. Flannery, S. Teukolsky, W. Vetterling, *Numerical Recipes*, Cambridge University Press, New York, 1986.
- [36] L. Yan, S. Hu, J.M. Duan, C.Y. Jing, J. Phys. Chem. A 118 (2014) 4759–4765.
- [37] J. Zhang, X. Chen, K. Takanabe, K. Maeda, K. Domen, J.D. Epping, X. Fu, M. Antonietti, X. Wang, Angew. Chem. Int. Ed. 49 (2010) 441–444.
- [38] J. Xu, T.J. Brenner, Z. Chen, D. Neher, M. Antonietti, M. Shalom, ACS Appl. Mater. Interfaces 6 (2014) 16481–16486.
- [39] P.V. Zinin, L.-C. Ming, S.K. Sharma, V.N. Khabashesku, X. Liu, S. Hong, S. Endo, T. Acosta, Chem. Phys. Lett. 472 (2009) 69–73.
- [40] X.-H. Li, X. Wang, M. Antonietti, ACS Catal. 2 (2012) 2082–2086.
- [41] X. Wang, S. Blechert, M. Antonietti, ACS Catal. 2 (2012) 1596–1606.